Numerical simulation of THz-wave-assisted electron diffraction for ultrafast molecular imaging

Reika Kanya and Kaoru Yamanouchi[*]

Department of Chemistry, School of Science, the University of Tokyo, 7-3-1 Hongo, Bunkyo-ku, Tokyo 113-0033, Japan

(Received 29 November 2016; published 16 March 2017)

A scheme for achieving high temporal resolution in gas electron diffraction is proposed, in which time-dependent electron diffraction patterns can be obtained from energy-resolved angular distributions of electrons scattered by molecules in dynamical processes under the presence of a single-cycle THz-wave pulse. Derived formulae of the differential cross section and numerical simulations of electron signals scattered by Ar atoms and Cl_2 molecules show that the temporal resolution of the proposed method can be <10 fs in the pump-probe measurement without scanning the time delay.

I. INTRODUCTION

One of the most challenging themes in molecular science is to probe ultrafast changes in geometrical structures of isolated molecules in real time with atomic-scale spatial resolution. Time-resolved gas electron diffraction with ultrashort electron pulses with a kinetic energy of $\sim 10^1$ kV has revealed molecular dynamics in the time scale of 10^{-9}–10^{-12} s [1–6]. Furthermore, several pioneering attempts have been made for achieving the femtosecond temporal resolution by newly developed experimental methods, such as electron diffraction with relativistic ultrashort electron pulses [7,8], x-ray diffraction with x-ray free electron lasers [9,10], and laser-induced electron diffraction with recolliding electrons in intense laser fields [11–13], as reviewed in Ref. [14].

Recently, we proposed a method called laser-assisted electron diffraction (LAED) [15], in which sub-10 fs temporal resolution can be achieved by using a laser-assisted elastic electron scattering (LAES) process, in which scattered electrons gain or lose their kinetic energy through the elastic electron scattering in a laser field. Because the LAES process occurs only when the electron collides with the target atoms or molecules in the presence of a laser field, it can be utilized as an optical gating for electron diffraction signals with high temporal resolutions. In 2014, we demonstrated the feasibility of LAED by measuring the electron diffraction patterns of CCl_4 molecules at the instant of the irradiation of femtosecond laser pulses [16].

In the present study, we propose another electron diffraction method called THz-wave-assisted electron diffraction (TAED), which can be regarded as a variation of LAED. In the TAED method, a single-cycle THz-wave pulse acts as a streaking electric field in the course of the electron diffraction process, and a series of snapshots of electron diffraction patterns of isolated molecules can be recorded with temporal resolution as high as less than 10 fs. Therefore, by the TAED method we are able to record dynamical processes of molecules in real time in the pump-probe measurements without scanning the pump-probe delay time, or even without using a femtosecond electron pulse.

As described in Sec. II, by modifying the theory developed by Kroll and Watson [17], we formulate the differential cross

section of a LAES process in an ultrabroadband electromagnetic pulse, which can be realized by a single-cycle THz-wave pulse. Then, using the derived formula, we calculate the energy and angular distributions of LAES signals induced by a single-cycle THz-wave pulse and show that high temporal resolution better than 10 fs can in principle be achieved by a pump-probe measurement without varying the pump-probe delay. Finally, we demonstrate that the internuclear distances of a molecule can be determined with high precision by the TAED method by applying it to a space-fixed diatomic molecule.

II. THEORY

In 1973, Kroll and Watson [17] derived a formula of the differential cross section for electron scattering by a target potential in a continuous laser field, $\mathbf{F}_0 \cos \omega t$, as

$$\frac{d\sigma_{\mathrm{KW}}}{dE_{\mathrm{f}}d\Omega} = \sum_{n=-\infty}^{\infty} \frac{|\mathbf{k}_{\mathrm{f}}|}{|\mathbf{k}_{\mathrm{i}}|} \delta(E_{\mathrm{f}} - E_{\mathrm{i}} - n\hbar\omega) J_n^2(\mathbf{s} \cdot \boldsymbol{\alpha}_0) \frac{d\sigma_{\tilde{\mathbf{k}}_{\mathrm{f}}, \tilde{\mathbf{k}}_{\mathrm{i}}}^{\mathrm{el}}}{d\Omega},$$

$$(1)$$

where E_{i} and E_{f} are kinetic energies of the incident electron and the scattered electron, respectively, $\mathbf{k}_{\mathrm{i}}$ and $\mathbf{k}_{\mathrm{f}}$ are the wave vectors of the incident electron and the scattered electron, respectively, $\delta(x)$ is the delta function, $J_n(x)$ is the nth-order Bessel function of the first kind, $\mathbf{s}$ is the momentum transfer defined as $\mathbf{s} = \mathbf{k}_{\mathrm{i}} - \mathbf{k}_{\mathrm{f}}$, and $\boldsymbol{\alpha}_0 = e\mathbf{F}_0/(m_{\mathrm{e}}\omega^2)$, where e is unit charge and m_{e} is mass of electron, and $d\sigma_{\tilde{\mathbf{k}}_{\mathrm{f}}, \tilde{\mathbf{k}}_{\mathrm{i}}}^{\mathrm{el}}/d\Omega$ is a differential cross section of elastic scattering ($\tilde{\mathbf{k}}_{\mathrm{f}} \leftarrow \tilde{\mathbf{k}}_{\mathrm{i}}$) without a laser field, where $\tilde{\mathbf{k}}_{\mathrm{i}}$ and $\tilde{\mathbf{k}}_{\mathrm{f}}$ are defined as

$$\tilde{\mathbf{k}}_{\mathrm{i,f}} = \mathbf{k}_{\mathrm{i,f}} + \frac{nm_{\mathrm{e}}\omega}{\hbar\mathbf{s} \cdot \boldsymbol{\alpha}_0}\boldsymbol{\alpha}_0. \qquad (2)$$

In the Kroll-Watson theory, both of the electron-target interaction and the laser-electron interaction are treated nonperturbatively under the following four assumptions: (i) laser-target interaction is negligibly small, (ii) scattering is nonresonant in the absence of an electromagnetic field, (iii) photon energy ($\hbar\omega$) is much smaller than the kinetic energy of incident electrons (E_{i}), i.e., $\hbar\omega \ll E_{\mathrm{i}}$, which is referred to as the low-frequency approximation, and (iv) scattering can be treated in a semiclassical manner by the stationary phase approximation, which is applicable under the condition of $|n| < |\mathbf{s} \cdot \boldsymbol{\alpha}_0|$. It has been confirmed that the Kroll-Watson

---
[*]kaoru@chem.s.u-tokyo.ac.jp

formula shows good agreement with experimental results, as long as the assumptions (i)–(iv) are satisfied [18,19].

On the other hand, the Kroll-Watson formula of Eq. (1) should be modified in order to describe LAES processes with a single-cycle THz-wave pulse, which is not a continuous wave. Therefore, we modify the Kroll-Watson formula by replacing the continuous laser field, $\mathbf{F}_0 \cos \omega t$, with a laser field having a general functional form, $\mathbf{F}(t)$, and derive the differential cross section under the assumptions (i)–(iii) mentioned above as

$$\frac{d\sigma_{\mathrm{KW}}}{dE_{\mathrm{f}}d\Omega} = \frac{|\mathbf{k}_{\mathrm{f}}|}{|\mathbf{k}_{\mathrm{i}}|} \lim_{T \to \infty} \frac{1}{2\pi\hbar T} \left| \int_{-T/2}^{T/2} dt\, e^{-i\Delta(\mathbf{k}_{\mathrm{i}},\mathbf{k}_{\mathrm{f}},t)} f_{\tilde{\mathbf{k}}_{\mathrm{f}},\tilde{\mathbf{k}}_{\mathrm{i}}}^{\mathrm{el}}(t) \right|^2,$$

(3)

where $f_{\tilde{\mathbf{k}}_{\mathrm{f}},\tilde{\mathbf{k}}_{\mathrm{i}}}^{\mathrm{el}}(t)$ is a scattering amplitude of elastic scattering ($\tilde{\mathbf{k}}_{\mathrm{f}} \leftarrow \tilde{\mathbf{k}}_{\mathrm{i}}$) in the absence of an electromagnetic field, where $\tilde{\mathbf{k}}_{\mathrm{i}}$ and $\tilde{\mathbf{k}}_{\mathrm{f}}$ are defined as

$$\tilde{\mathbf{k}}_{\mathrm{i,f}} = \mathbf{k}_{\mathrm{i,f}} + \frac{e}{\hbar}\mathbf{A}(t),$$

(4)

and $\Delta(\mathbf{k}_{\mathrm{i}},\mathbf{k}_{\mathrm{f}},t)$ is defined as

$$\Delta(\mathbf{k}_{\mathrm{i}},\mathbf{k}_{\mathrm{f}},t) = \frac{E_{\mathrm{f}} - E_{\mathrm{i}}}{\hbar}t - \frac{e}{m_{\mathrm{e}}}\int_{-\infty}^{t} d\tau\, \mathbf{s}\cdot\mathbf{A}(\tau),$$

(5)

where $\mathbf{A}(t)$ is a vector potential. The details of the derivation are described in the Appendix. A formula similar to Eq. (3) was reported by Čerkić and Milošević [20] under the second Born approximation of the electron-target interaction, but it should be noted that, in the present formula of Eq. (3), all the Born series for the electron-target interaction are incorporated. It is worthy to note that Eq. (2) becomes identical to Eq. (4) under the semiclassical correspondence of $n = -\mathbf{s}\cdot\boldsymbol{\alpha}_0 \sin\omega t$ [17]. In Eq. (3), $f_{\tilde{\mathbf{k}}_{\mathrm{f}},\tilde{\mathbf{k}}_{\mathrm{i}}}^{\mathrm{el}}(t)$ is dependent on time because target molecules in dynamical processes are considered in the present study. When the assumption (iv), i.e., the stationary phase approximation, is applied to Eq. (3), the differential cross section is written as

$$\frac{d\sigma_{\mathrm{KW}}}{dE_{\mathrm{f}}d\Omega} = \frac{|\mathbf{k}_{\mathrm{f}}|}{|\mathbf{k}_{\mathrm{i}}|} \lim_{T \to \infty} \frac{1}{2\pi\hbar T} \left| \sum_j e^{-i\Delta(\mathbf{k}_{\mathrm{i}},\mathbf{k}_{\mathrm{f}},t_{\mathrm{c}}^{(j)})} \right.$$
$$\left. \times \sqrt{\frac{2\pi i m_{\mathrm{e}}}{e\left|\mathbf{s}\cdot\mathbf{F}(t_{\mathrm{c}}^{(j)})\right|}} f_{\tilde{\mathbf{k}}_{\mathrm{f}},\tilde{\mathbf{k}}_{\mathrm{i}}}^{\mathrm{el}}(t_{\mathrm{c}}^{(j)}) \right|^2,$$

(6)

where $t_{\mathrm{c}}^{(j)}$ is a collision time when the projectile electron collides with the target and is determined by

$$\Delta E = \left\{ \frac{\hbar}{m_{\mathrm{e}}} e A(t_{\mathrm{c}}^{(j)}) \right\} s_{\parallel},$$

(7)

where $A(t) = |\mathbf{A}(t)|$, ΔE is an energy shift defined as $\Delta E = E_{\mathrm{f}} - E_{\mathrm{i}}$, and $s_{\parallel}$ is a momentum transfer along the polarization vector, $s_{\parallel} = \mathbf{s}\cdot\mathbf{F}(t)/|\mathbf{F}(t)|$. Equation (6) shows that the scattering amplitude is expressed as a sum of the contributions from all the collision times, which determine the ratio of ΔE and $s_{\parallel}$ of the scattering processes through Eq. (7). Although Eqs. (6) and (7) give us an intuitive description of THz-wave-assisted electron scattering (TAES) processes as well as the relationship among the scattering angle, the energy shift, and the collision time of scattered electrons, the singularities appearing at
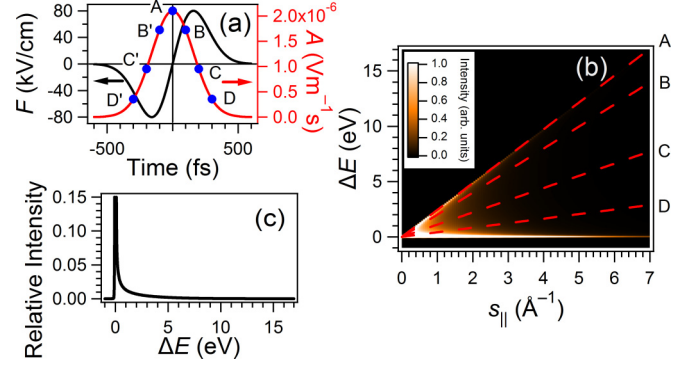

FIG. 1. (a) THz pulse in the present simulation. Black solid line: Electric field. Red solid line: Vector potential. (b) Signal distribution of electrons scattered by Ar atoms. (c) Energy spectrum of scattered electrons.

$\mathbf{s}\cdot\mathbf{F}(t_{\mathrm{c}}^{(j)}) = 0$ in Eq. (6) would introduce significant errors in numerical calculations. Therefore, the original equation, Eq. (3), was adopted in the present numerical calculations of the TAES processes, and Eqs. (6) and (7) were adopted in the analysis and interpretation of the numerical results.

III. RESULTS AND DISCUSSION

In the simulations, the kinetic energy of the incident electron is set to be 1.0 keV, and the electric field of a single-cycle THz pulse is assumed to be expressed as

$$\mathbf{F}(t) = F_0 \omega_0 t \exp\left[-\frac{\omega_0^2 t^2 - 1}{2} \right],$$

(8)

where the peak electric field intensity (F_0) is 0.08 MV/cm and the peak frequency (ω_0) is 1.0 THz. The black solid line and the red solid line shown in Fig. 1(a) are the electric field and the vector potential of the THz pulse employed in the simulations, respectively.

By using Eq. (3), we calculated electron scattering intensities by Ar atoms in the single-cycle THz pulse. In the simulation, $f_{\tilde{\mathbf{k}}_{\mathrm{f}},\tilde{\mathbf{k}}_{\mathrm{i}}}^{\mathrm{el}}$ for Ar atoms in the absence of an electromagnetic field was adopted from Ref. [21]. Figure 1(b) shows the electron scattering intensities as a function of the momentum transfer along the polarization vector $s_{\parallel}$ and the energy shift ΔE. The energy shift of 17 eV corresponds to the photon number of around 4×10^3 for the THz wave whose frequency is 1.0 THz. The original intensity image directly obtained from Eq. (3) exhibits an interference structure along the energy shift axis with a small period of about 0.01–0.1 eV, which is originated from the two different collision times as explained below. Considering that this fine interference structure could not be resolved in the measurements using a typical LAES apparatus with an electron beam whose incident energy is around 1 keV [22], we average the original scattering intensity pattern over the energy shift axis by a Gaussian convolution function having the width of 0.1 eV (FWHM) to obtain the scattering intensity pattern shown in Fig. 1(b).

As represented by Eq. (7), ΔE increases linearly when $s_{\parallel}$ increases, and its slope is proportional to the vector potential

$A(t_c)$ at the collision time t_c. For example, at $A(0\,\text{fs}) = 2.10 \times 10^{-6}\,\text{V}\,\text{m}^{-1}\,\text{s}$, represented as the point A in Fig. 1(a), the corresponding signals of the scattering amplitude are distributed along the straight line of $\Delta E = 2.43\,[\text{eV}\,\text{Å}] \times s_\parallel$, shown as the broken line A in Fig. 1(b). At the collision times of $t_c = +100\,\text{fs}$ and $t_c = -100\,\text{fs}$, the vector potentials become smaller than at $t_c = 0$, as represented as the points B and B′ in Fig. 1(a), and the corresponding signals appear along the broken line B in Fig. 1(b), exhibiting the shallower slope than at $t_c = 0\,\text{fs}$. Similarly, the vector potentials at the collision times at $t_c = \pm 200\,\text{fs}$ are represented as the points C and C′ in Fig. 1(a), and the corresponding signals appear along the broken line C in Fig. 1(b), whose slope is even shallower than the broken line B.

As explained above, the scattering amplitude consists of the contributions of electron scattering at two collision times, i.e., $t = \pm t_c$, except for $t = 0$, and the two contributions can form an interference structure in the scattering amplitude. The fine interference structures appearing along the energy shift axis with the spacing less than $\sim 0.1\,\text{eV}$ before the convolution averaging originate from this interference. Because the interference term appearing as the cross term of $e^{-i\{\Delta(\mathbf{k}_i, \mathbf{k}_f, t_c^{(j)}) - \Delta(\mathbf{k}_i, \mathbf{k}_f, -t_c^{(j)})\}} f^{\text{el}}_{\tilde{\mathbf{k}}_f, \tilde{\mathbf{k}}_i}(t_c^{(j)}) f^{\text{el}*}_{\tilde{\mathbf{k}}_f, \tilde{\mathbf{k}}_i}(-t_c^{(j)}) + \text{c.c.}$ in the differential cross section of Eq. (6) is smeared out by the convolution process, the convoluted differential cross section, $\langle d\sigma_{\text{KW}}/dE_f d\Omega \rangle_{\text{conv}}$, shown in Fig. 1(b), can be approximated as an incoherent sum of scattering intensities at $t = +t_c$ and $t = -t_c$, i.e.,

$$
\left\langle \frac{d\sigma_{\text{KW}}}{dE_f d\Omega} \right\rangle_{\text{conv}} \approx \left\langle \frac{|\mathbf{k}_f|}{|\mathbf{k}_i|} \lim_{T \to \infty} \sum_j \frac{m_e}{\hbar T e |\mathbf{s} \cdot \mathbf{F}(t_c^{(j)})|} \right.
$$
$$
\left. \times \left[|f^{\text{el}}_{\tilde{\mathbf{k}}_f, \tilde{\mathbf{k}}_i}(-t_c^{(j)})|^2 + |f^{\text{el}}_{\tilde{\mathbf{k}}_f, \tilde{\mathbf{k}}_i}(t_c^{(j)})|^2 \right] \right\rangle_{\text{conv}},
$$
(9)

where $\langle \ \rangle_{\text{conv}}$ represents the convolution.

Figure 1(c) shows the energy spectrum obtained by the integration of the electron signals along the $s_\parallel$ axis in Fig. 1(b). The signal intensity of the spectrum is normalized with respect to the peak intensity of the elastic scattering signal, i.e., the peak intensity at $\Delta E = 0\,\text{eV}$ obtained by assuming that the electron pulse has a rectangular temporal profile with the width of 3 ps. As shown in Fig. 1(c), the intensities of the energy-shifted signals at 0.1 eV and 10.0 eV are 1.3×10^{-1} and 3.1×10^{-4}, respectively. Because the LAES signals with the intensity of around 10^{-4}, which was also normalized with respect to the peak intensity of the elastic scattering signal, were detected with a sufficiently high signal-to-noise ratio in our previous study [23], the intensity of the expected TAES signals in Fig. 1(b) shows that the TAES signals can appear sufficiently above the detection limit.

In order to demonstrate the application of TAES processes to ultrafast gas electron diffraction, we performed a model calculation of TAES signals from a space-fixed Cl_2 molecule using the THz pulse shown in Fig. 1(a). As shown in Fig. 2(a), the molecular axis is set to be parallel to the polarization direction of the THz field, and the direction of the incident electron beam is set to be perpendicular to the molecular axis. In the simulation, the internuclear distance of the Cl_2
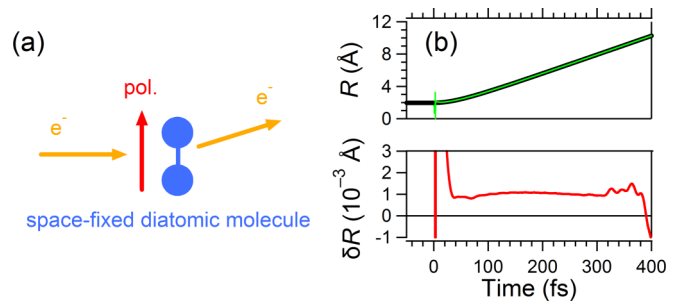

FIG. 2. (a) Schematic of the scattering configuration. (b, Top panel) Black thick solid line: The initially given temporal dependence of the internuclear distance (R) of the dissociating Cl_2 molecule. Green thin solid line: The time-dependent internuclear distance retrieved from $I_{\text{pos}}(s_\parallel, t_c)$ shown in Fig. 3(e). (b, Bottom panel) Red solid line: The deviations of the retrieved internuclear distance from the initially given internuclear distance.

molecule is fixed at the equilibrium internuclear distance (R_e), $R_e = 1.98\,\text{Å}$ [24]. The scattering amplitude for Cl_2 in the absence of an electromagnetic field was evaluated on the basis of the independent atom model, in which $f^{\text{el}}_{\tilde{\mathbf{k}}_f, \tilde{\mathbf{k}}_i}$ for a Cl atom was adopted from Ref. [21]. Figure 3(a) shows the resultant electron scattering signals from Cl_2. Although entire signal distribution is similar to that in Fig. 1(b), a characteristic electron diffraction pattern can be seen along the $s_\parallel$ axis.

The effect of the thermal distribution of the internuclear distance can be included into the current analysis by using the same procedure as in the analysis of a conventional gas electron diffraction pattern [25]. Using the mean amplitude (l_h) of Cl_2, $l_h = 0.044\,\text{Å}$ [24], at 300 K, it is confirmed that the effect of the molecular vibration appears as a damping of the diffraction pattern only by 5% even at $7\,\text{Å}^{-1}$ in Fig. 3(a).

Next, we simulated electron scattering signals from dissociating Cl_2 molecules. The molecule starts to dissociate at $t = 0\,\text{fs}$, and the temporal variation of the internuclear distance, R, was calculated by a classical trajectory simulation on a potential energy curve whose shape is assumed to be represented by $V(R) = E_{\text{RKE}}(R_e/R)^3$, where $E_{\text{RKE}} = 0.5\,\text{eV}$, representing the kinetic energy released when $R = R_e$, the equilibrium internuclear distance of Cl_2 in the electronic ground state. The obtained temporal variation of the internuclear distance is shown as the black thick solid line in the top panel of Fig. 2(b). Figure 3(b) shows the resultant electron scattering signals for the dissociating Cl_2.

By the transformation of ΔE into $|t_c|$ by using Eqs. (7) and (8), Figs. 3(a) and 3(b) can be converted into Figs. 3(c) and 3(d), respectively. The electron diffraction pattern in Fig. 3(c) is constant with respect to $|t_c|$, reflecting the constant internuclear distance. On the other hand, the diffraction pattern in Fig. 3(d) has two components, i.e., (i) the constant pattern originating from the electron diffraction in the negative collision times during which the internuclear distance does not vary, and (ii) the pattern varying as a function of time originated from the electron diffraction in the positive collision times during which the internuclear distance becomes longer, as shown in the top panel of Fig. 2(b). The constant pattern (i) above should be the same as the diffraction pattern in Fig. 3(c), but its intensity should be half of the pattern in Fig. 3(c)
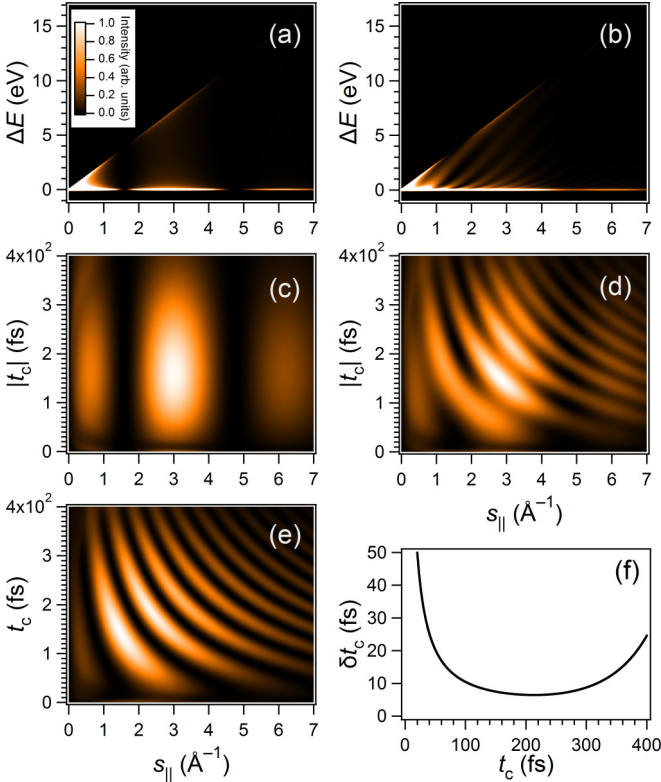
FIG. 3. (a, b) Signal distributions of electrons scattered by rigid and dissociating Cl_2 molecules, respectively. (c, d) Signal distributions of electrons scattered by rigid and dissociating Cl_2 molecules, respectively, as a function of the momentum transfer and the absolute value of the collision time. (e) Signal distribution of electrons scattered by dissociating Cl_2 molecules as a function of the momentum transfer and the collision time. (f) The temporal resolutions of the collision time as a function of t_c by assuming $s_\parallel = 5.0\,\text{Å}^{-1}$, $\delta(\Delta E) = 0.2\,\text{eV}$, $\delta s_\parallel/s_\parallel = 2\%$, and $\delta A/A = 3\%$. The color scales for (b)–(e) are the same as that for (a).

because the pattern in Fig. 3(c) is the incoherent sum of the same contributions in the positive and negative collision times. Therefore, the time-dependent electron diffraction pattern for the positive collision time $[I_{pos}(s_\parallel, t_c)]$ is obtained as shown in Fig. 3(e) by subtracting the contribution of the negative collision time, that is, the half of the signal intensity of Cl_2 at $R = R_e$ shown in Fig. 3(c), from the intensity distribution in Fig. 3(d).

The horizontal slices at t_c in Fig. 3(e) show the electron diffraction pattern originating from the interference of the two scattering waves generated at the two nuclei in Cl_2, and the spacing between the adjacent intensity peaks becomes smaller as the internuclear distance becomes larger. Therefore, Fig. 3(e) shows that the internuclear distance increases as a function of the collision time and that the chemical bond stretching motion, which eventually leads to the chemical bond breaking, can be recorded as a time-dependent diffraction pattern by the TAED measurement without scanning the pump-probe delay. Because the electron signals shown in Figs. 3(a) and 3(b) were obtained through the convolution along the energy shift axis, the collision time in Fig. 3(e), which is converted from δE and $s_\parallel$, also carries uncertainties.

From Eq. (7), when $F(t)$ is defined as $F(t) = |\mathbf{F}(t)|$,

$$\frac{dt_c}{d(\Delta E)} = -\frac{m_e}{\hbar e s_\parallel F(t_c)} \qquad (10)$$

is obtained, showing that the uncertainty in t_c becomes large when $F(t_c)$ and/or $s_\parallel$ take small values. As shown in Fig. 1(a), $F(t_c)$ becomes small at $t_c \approx 0$ fs and $t_c > 400$ fs. Consequently, the temporal resolution of the electron scattering signals around $t_c \approx 0$ fs and $t_c > 400$ fs becomes low. In addition, when $s_\parallel \approx 0\,\text{Å}^{-1}$, the temporal resolution also becomes low.

The procedure of the analysis of $I_{pos}(s_\parallel, t_c)$ is the same as that in the conventional gas electron diffraction. By using the molecular scattering intensity expressed as

$$\cos(s_\parallel r) \propto \frac{I_{pos}(s_\parallel, t_c) - I_a(s_\parallel)}{I_a(s_\parallel)}, \qquad (11)$$

where $I_a(s_\parallel)$ is the sum of the TAES signals scattered by each constituent atom, the internuclear distance R at each collision time can be obtained from the least-squares fitting of the right-hand side of Eq. (10) to the cosine function. The green thin solid line in the top panel of Fig. 2(b) shows the temporal evolution of the internuclear distance, which was obtained from $I_{pos}(s_\parallel, t_c)$, shown in Fig. 3(e), by excluding the small $s_\parallel$ region of $s_\parallel < 0.3\,\text{Å}^{-1}$. The temporal evolution of the internuclear distance in the range of $t_c \geqslant 3.4$ fs shows good agreement with the classical dissociation trajectory represented by the black thick solid line in Fig. 2(b). The red solid line in the bottom panel of Fig. 2(b) shows the deviation of the internuclear distance (δR), which is calculated through the subtraction of the initially given internuclear distance from the retrieved internuclear distance. It is found that the discrepancies are less than 0.0015 Å, which is sufficiently small, in the temporal range of $t_c \geqslant 30$ fs. On the other hand, in the temporal range of $t_c < 3.4$ fs, the least-squares fitting with a single internuclear distance gives large residuals because of insufficient temporal resolutions around $t_c = 0$ fs, as discussed above.

It is true that the random orientation of molecules decreases the visibility of the diffraction pattern, which is defined as $\Delta I/I_{ave}$, where ΔI is the amplitude of the diffraction pattern and I_{ave} is the average of the baseline scattering intensities with respect to which the diffraction pattern appears. For example, the visibility of almost 100% at around $s_\parallel = 5\,\text{Å}^{-1}$ in Fig. 3(c) decreases to $\sim$10% for a randomly oriented ensemble of Cl_2 molecules. The analysis of diffraction patterns of randomly oriented molecules is basically the same as that described in Ref. [25].

Because single-cycle THz pulses with the peak electric field strength of 1.2 MV/cm can be achieved [26] by the method of tilted-pulse-front pumping [27], the field intensity of 0.08 MV/cm adopted in the present simulation can be generated with no experimental difficulties. The temporal shape of the vector potential appearing in Eq. (7) can be obtained from the time-dependent electric fields of THz pulses, which can be measured by well-established methods such as the photoconductive sampling method [28] and the electro-optical sampling method [29]. We have already demonstrated simultaneous measurements of the energy and angular distributions

of scattered electrons in LAES processes [15,16,22,23]. Therefore, there will be no substantial difficulties in future experimental demonstrations of the TAED method.

From the relationship of Eq. (7), the temporal resolution (δt_c) of the TAED method is evaluated as

$$\delta t_c = \sqrt{\left\{\frac{A(t_c)\delta s_\parallel}{F(t_c)s_\parallel}\right\}^2 + \left\{\frac{\delta A(t_c)}{F(t_c)}\right\}^2 + \left\{\frac{m_e\delta(\Delta E)}{\hbar e s_\parallel F(t_c)}\right\}^2}, \quad (12)$$

where $\delta s_\parallel$, δA, and $\delta(\Delta E)$ are experimental errors in the momentum transfer, the vector potential, and the energy shift, respectively. For example, Fig. 3(f) shows δt_c estimated from Eq. (11) as a function of t_c by assuming the following conditions: $s_\parallel = 5.0\,\text{Å}^{-1}$, $\delta(\Delta E) = 0.2\,\text{eV}$, $\delta s_\parallel/s_\parallel = 2\%$, and $\delta A/A = 3\%$. The best resolution is found to be $\delta t_c = 6.4$ fs, which is achieved at around $t_c = 210$ fs, and the temporal resolution is better than 10 fs in the range of $105\,\text{fs} \leqslant t_c \leqslant 317\,\text{fs}$, showing that time-resolved electron diffraction patterns with sub-10 fs temporal resolution can be achieved by the TAED method. As shown in Fig. 3(f), the temporal resolution becomes significantly low at around $t_c = 0$ fs. Therefore, in pump-probe measurements in which an ultrashort pump laser pulse induces dynamical processes of molecules and a single-cycle THz-wave pulse probes the dynamics, the timing between the pump and probe pulses needs to be chosen so that the highest temporal resolution is achieved in a time domain of interest. As described in Eq. (12), the temporal resolution is also dependent on $s_\parallel$ and becomes significantly low at small $s_\parallel$. However, by excluding the electron signals in the small $s_\parallel$ region from the structural analyses, high temporal resolutions in the structural determination can be secured in the TAED method, as demonstrated by the retrieval of the internuclear distance as a function of time shown in Fig. 2(b).

Among the experimental conditions discussed above, the intensity fluctuation of $\delta A/A = 3\%$ seems to be the most demanding requirement. However, (i) the shot-by-shot fluctuation of the THz field can be calibrated by the coincidence measurement of the THz pulse intensity and the electron signals, and (ii) the spatial variation of the THz field can be suppressed by the loosely focused condition or the flat-top focal spot by using a designed focusing mirror for the THz pulses.

IV. CONCLUSION

In conclusion, we have proposed the TAED method for probing geometrical structures of isolated molecules with sub-10 fs temporal resolution and have formulated the differential cross section of LAES processes induced by ultrabroadband pulses. The feasibility of the proposed method was confirmed by the numerical simulations for the target atomic and molecular species, Ar and Cl_2. The TAED method has the following advantages: (i) sub-10 fs temporal resolutions can be achieved without scanning the pump-probe delay and (ii) generation of femtosecond electron pulses is not required for achieving femtosecond temporal resolutions. Furthermore, in the TAED method, THz waves would not induce any vibrational or electronic excitations of target molecules in the dynamical processes because their wavelength is far off-resonance and their intensities at around 10^7 W/cm^2 are sufficiently low,

which is in contrast to the laser-induced electron diffraction method where molecules are exposed to a mid-infrared laser field whose intensity is around 10^{13} W/cm^2 or larger [11–13]. Although some discrepancies were previously found between the experiments and the Kroll-Watson theory in the LAES processes with the laser field intensities larger than 10^{11} W/cm^2 [16,23], it was recently confirmed that the Kroll-Watson theory shows good agreement with the experimental results as long as the laser field intensities are less than 10^{10} W/cm^2 [30–33]. Therefore, the present theoretical treatment based on the Kroll-Watson theory is expected to be applicable to the analyses of experimental data to be obtained by TAED experiments, which will be performed at intensities of around 10^7 W/cm^2.

The attosecond streaking of photoionization processes [34,35], in which a few-cycle laser pulse acts as a streaking field for electrons emitted through photoionization processes of atoms and molecules, is similar to the present TAED method in the sense that collision time is retrieved from the energy and momentum of electrons by the streaking technique. The present study demonstrated that the scattering process of external electrons by atoms and molecules can also be investigated by the streaking technique.

The present idea of the streaking of electron scattering processes can be also applied to LAES induced by few-cycle laser pulses. It is possible that attosecond temporal resolution is achieved in electron-atom collisions by the streaking of the scattered electrons by a few-cycle laser pulse.

APPENDIX

The derivation of Eq. (3) is basically the same as that of Eq. (1) reported by Kroll and Watson [17], and the only difference is the use of a laser field having a general functional form, $\mathbf{F}(t)$, in this study instead of that having a functional form of $\mathbf{F}_0 \cos\omega t$ in Ref. [17]. In this Appendix, the derivation of Eq. (3) is described.

The S-matrix ($S_{f,i}$) of the LAES process scattered by a potential $V(\mathbf{r},t)$ is written as

$$S_{f,i} = \delta(\mathbf{k}_f - \mathbf{k}_i) - \frac{i}{\hbar}\iint d\mathbf{r}\,dt\,\chi^*_{\mathbf{k}_f}(\mathbf{r}, t)V(\mathbf{r}, t)\varphi_{\mathbf{k}_i}(\mathbf{r}, t),$$

(A1)

where $\varphi_\mathbf{k}(\mathbf{r}, t)$ is the exact wave function of the scattering process and satisfies

$$\varphi_\mathbf{k}(\mathbf{r}, t) = \chi_\mathbf{k}(\mathbf{r}, t) + \iint d\mathbf{r}'\,dt'\,g^{(+)}(\mathbf{r}, t; \mathbf{r}', t')V(\mathbf{r}', t')\varphi_\mathbf{k}(\mathbf{r}, t).$$

(A2)

In Eq. (A2), $\chi_\mathbf{k}(\mathbf{r}, t)$ is the exact wave function of a free electron in a laser electric field $\mathbf{F}(t)$, which is called the Volkov solution, expressed as

$$\chi_\mathbf{k}(\mathbf{r}, t) = (2\pi)^{-3/2}e^{-i[\eta(\mathbf{k}, t) - \mathbf{k}\cdot\mathbf{r}]},$$

(A3)

where

$$\eta(\mathbf{k}, t) = \frac{E_k}{\hbar} t + \frac{e}{m_e} \int_{-\infty}^{t} d\tau \, \mathbf{k} \cdot \mathbf{A}(\tau), \qquad (\text{A4})$$

and $g^{(+)}(\mathbf{r}, t; \mathbf{r}', t')$ is the Green function of a free electron in the laser electric field defined as

$$g^{(+)}(\mathbf{r}, t; \mathbf{r}', t') = \frac{1}{i\hbar} \Theta(t - t') \int d\mathbf{k}' \chi_{\mathbf{k}'}^*(\mathbf{r}, t) \chi_{\mathbf{k}'}(\mathbf{r}', t'), \qquad (\text{A5})$$

where $\Theta(x)$ is the Heaviside step function. Next, a function $\bar{\varphi}_{\mathbf{k}}(\boldsymbol{\kappa}, t)$, defined as

$$\bar{\varphi}_{\mathbf{k}}(\boldsymbol{\kappa}, t) = e^{i\eta(\mathbf{k}, t)} \tilde{\varphi}_{\mathbf{k}}(\boldsymbol{\kappa}, t), \qquad (\text{A6})$$

is introduced, where $\tilde{\varphi}_{\mathbf{k}}(\boldsymbol{\kappa}, t)$ is the Fourier transform of $\varphi_{\mathbf{k}}(\mathbf{r}, t)$ with respect to space. Similarly, $\bar{\chi}_{\mathbf{k}}(\boldsymbol{\kappa}, t)$, defined as

$$\bar{\chi}_{\mathbf{k}}(\boldsymbol{\kappa}, t) = e^{i\eta(\mathbf{k}, t)} \tilde{\chi}_{\mathbf{k}}(\boldsymbol{\kappa}, t) = \delta(\boldsymbol{\kappa} - \mathbf{k}), \qquad (\text{A7})$$

is introduced. By using Eqs. (A2), (A5), (A6), and (A7),

$$\bar{\varphi}_{\mathbf{k}_i}(\boldsymbol{\kappa}, t) = \delta(\boldsymbol{\kappa} - \mathbf{k}_i) + \frac{e^{-i\Delta(\mathbf{k}_i, \boldsymbol{\kappa}, t)}}{i\hbar} \int_{-\infty}^{t} dt' e^{i\Delta(\mathbf{k}_i, \boldsymbol{\kappa}, t')}$$
$$\times \int d\boldsymbol{\kappa}' \tilde{V}(\boldsymbol{\kappa} - \boldsymbol{\kappa}', t') \bar{\varphi}_{\mathbf{k}_i}(\boldsymbol{\kappa}', t') \qquad (\text{A8})$$

is obtained. Equation (A8) can be expressed as

$$\bar{\varphi}_{\mathbf{k}_i}(\boldsymbol{\kappa}, t) = \sum_{n=0}^{\infty} \bar{\varphi}_{\mathbf{k}_i}^{(n)}(\boldsymbol{\kappa}, t), \qquad (\text{A9})$$

where

$$\bar{\varphi}_{\mathbf{k}_i}^{(0)}(\boldsymbol{\kappa}, t) = \delta(\boldsymbol{\kappa} - \mathbf{k}_i), \qquad (\text{A10})$$

$$\bar{\varphi}_{\mathbf{k}_i}^{(n+1)}(\boldsymbol{\kappa}, t) = \frac{e^{-i\Delta(\mathbf{k}_i, \boldsymbol{\kappa}, t)}}{i\hbar} \int_{-\infty}^{t} dt' e^{i\Delta(\mathbf{k}_i, \boldsymbol{\kappa}, t')}$$
$$\times \int d\boldsymbol{\kappa}' \tilde{V}(\boldsymbol{\kappa} - \boldsymbol{\kappa}', t') \bar{\varphi}_{\mathbf{k}_i}^{(n)}(\boldsymbol{\kappa}', t'). \qquad (\text{A11})$$

Because the interaction time between the high-energy incident electron and the target atom or molecule is much shorter than the time scale of the variation of the scattering potential, $\tilde{V}(\boldsymbol{\kappa} - \boldsymbol{\kappa}', t')$ can be regarded to be constant in time in the evaluation of the integral with respect to t' in Eq. (A11). Furthermore, when the low-frequency approximation, i.e., $\hbar\omega \ll E_i$, is adopted,

$$\left| \frac{\partial \bar{\varphi}_{\mathbf{k}_i}^{(n)}(\boldsymbol{\kappa}, t)}{\partial t} \right| \ll \left| \dot{\Delta} \bar{\varphi}_{\mathbf{k}_i}^{(n)}(\boldsymbol{\kappa}, t) \right| \qquad (\text{A12})$$

and

$$\left| \ddot{\Delta}(\mathbf{k}_i, \boldsymbol{\kappa}, t) \right| \ll \dot{\Delta}(\mathbf{k}_i, \boldsymbol{\kappa}, t)^2 \qquad (\text{A13})$$

are satisfied, where the dot above $\Delta(\mathbf{k}_i, \boldsymbol{\kappa}, t)$ represents the derivative with respect to time. Then, from the relationship of

$$\frac{\partial}{\partial t'} \left[\frac{e^{i\Delta(\mathbf{k}_i, \boldsymbol{\kappa}, t')} \tilde{V}(\boldsymbol{\kappa} - \boldsymbol{\kappa}', t') \bar{\varphi}_{\mathbf{k}_i}^{(n)}(\boldsymbol{\kappa}', t')}{i\dot{\Delta}(\mathbf{k}_i, \boldsymbol{\kappa}, t')} \right]$$
$$\approx e^{i\Delta(\mathbf{k}_i, \boldsymbol{\kappa}, t')} \tilde{V}(\boldsymbol{\kappa} - \boldsymbol{\kappa}', t') \bar{\varphi}_{\mathbf{k}_i}^{(n)}(\boldsymbol{\kappa}', t'), \qquad (\text{A14})$$

Eq. (A11) can be evaluated by

$$\bar{\varphi}_{\mathbf{k}_i}^{(n+1)}(\boldsymbol{\kappa}, t) \approx -\frac{1}{\hbar\dot{\Delta}(\mathbf{k}_i, \boldsymbol{\kappa}, t)} \int d\boldsymbol{\kappa}' \tilde{V}(\boldsymbol{\kappa} - \boldsymbol{\kappa}', t) \bar{\varphi}_{\mathbf{k}_i}^{(n)}(\boldsymbol{\kappa}', t).$$
$$(\text{A15})$$

Equation (A15) shows that the time t can be regarded as a parameter in the collision process because the interaction time between the electron and the target, which is around several attoseconds or shorter, is much shorter than both of the period of the laser field and the time scale of the variation of the scattering potential. Since

$$-\frac{1}{\hbar\dot{\Delta}(\mathbf{k}_i, \boldsymbol{\kappa}, t)} = \left(\frac{\hbar^2}{2m_e} |\tilde{\mathbf{k}}_i|^2 - \frac{\hbar^2}{2m_e} |\tilde{\kappa}|^2 \right)^{-1} \qquad (\text{A16})$$

holds, where $\tilde{\mathbf{k}}_i$ and $\tilde{\kappa}$ are defined in the same manner as in Eq. (4),

$$\bar{\varphi}_{\mathbf{k}_i}(\boldsymbol{\kappa}, t) = \tilde{\varphi}_{\tilde{\mathbf{k}}_i}^{\text{el}}(\tilde{\kappa}) \qquad (\text{A17})$$

is derived, where $\tilde{\varphi}_{\tilde{\mathbf{k}}_i}^{\text{el}}(\tilde{\kappa})$ is the exact wave function in the momentum space for the elastic scattering process of $\tilde{\kappa} \leftarrow \tilde{\mathbf{k}}_i$ in the absence of an electromagnetic field. By using Eqs. (A1), (A3), (A6), and (A17),

$$S_{\text{f,i}} - \delta(\mathbf{k}_f - \mathbf{k}_i) = -\frac{i}{8\pi^3\hbar} \int dt \, e^{-i\Delta(\mathbf{k}_i, \mathbf{k}_f, t)} \int d\boldsymbol{\kappa}$$
$$\times \int d\mathbf{r} \, e^{-i(\mathbf{k}_f - \boldsymbol{\kappa})\cdot\mathbf{r}} V(\mathbf{r}, t) \tilde{\varphi}_{\tilde{\mathbf{k}}_i}^{\text{el}}(\tilde{\kappa})$$
$$= -\frac{i}{(2\pi)^{3/2}\hbar} \int dt \, e^{-i\Delta(\mathbf{k}_i, \mathbf{k}_f, t)}$$
$$\times \int d\boldsymbol{\kappa} \, V(\tilde{\mathbf{k}}_f - \tilde{\kappa}, t) \tilde{\varphi}_{\tilde{\mathbf{k}}_i}^{\text{el}}(\tilde{\kappa})$$
$$= \frac{i\hbar}{4\pi^2 m_e} \int dt \, e^{-i\Delta(\mathbf{k}_i, \mathbf{k}_f, t)} f_{\tilde{\mathbf{k}}_f, \tilde{\mathbf{k}}_i}^{\text{el}}(t) \qquad (\text{A18})$$

is obtained, and thus Eq. (3) can be derived as

$$\frac{d\sigma_{\text{KW}}}{dE_f d\Omega} = \frac{8\pi^3 m_e^2 |\mathbf{k}_f|}{\hbar^3 |\mathbf{k}_i|} \lim_{T \to \infty} \frac{1}{T} |S - \delta(\mathbf{k}_f - \mathbf{k}_i)|^2$$
$$= \frac{|\mathbf{k}_f|}{|\mathbf{k}_i|} \lim_{T \to \infty} \frac{1}{2\pi\hbar T} \left| \int_{-T2}^{T2} dt \, e^{-i\Delta(\mathbf{k}_i, \mathbf{k}_f, t)} f_{\tilde{\mathbf{k}}_f, \tilde{\mathbf{k}}_i}^{\text{el}}(t) \right|^2. \qquad (\text{A19})$$

Because the time dependence in $f_{\tilde{\mathbf{k}}_f, \tilde{\mathbf{k}}_i}^{\text{el}}(t)$ is originated mainly from the change in the geometrical structures of target molecules in the high-energy electron scattering without resonances, the time scale of the change is of the order of 10^1–10^2 fs. On the other hand, over most of the integration range of $-T/2 \leqslant t \leqslant T/2$ in Eq. (A19), the exponential factor oscillates much faster than $f_{\tilde{\mathbf{k}}_f, \tilde{\mathbf{k}}_i}^{\text{el}}(t)$ at the period around 10^{-1}–10^0 fs. Therefore, the integral with respect to time in Eq. (A19) can be evaluated with the stationary phase approximation, and consequently, Eq. (6) can be obtained.

[1] H. Ihee, V. A. Lobastov, U. Gomez, B. M. Goodson, R. Srinivasan, C.-Y. Ruan, and A. H. Zewail, Direct imaging of transient molecular structures with ultrafast diffraction, Science **291**, 458 (2001).

[2] R. C. Dudek and P. M. Weber, Ultrafast diffraction imaging of the electrocyclic ring-opening reaction of 1,3-cyclohexadiene, J. Phys. Chem. A **105**, 4167 (2001).

[3] K. Hoshina, K. Yamanouchi, T. Ohshima, Y. Ose, and H. Todokoro, Direct observation of molecular alignment in an intense laser field by pulsed gas electron diffraction, I: Observation of anisotropic diffraction image, Chem. Phys. Lett. **353**, 27 (2002).

[4] R. Srinivasan, V. A. Lobastov, C.-Y. Ruan, and A. H. Zewail, Ultrafast electron diffraction (UED): A new development for the 4D determination of transient molecular structures, Helv. Chim. Acta **86**, 1763 (2003).

[5] R. Srinivasan, J. S. Feenstra, S. T. Park, S. Xu, and A. H. Zewail, Dark structures in molecular radiationless transitions determined by ultrafast diffraction, Science **307**, 558 (2005).

[6] J. Yang, J. Beck, C. J. Uiterwaal, and M. Centurion, Imaging of alignment and structural changes of carbon disulfide molecules using ultrafast electron diffraction, Nat. Commun. **6**, 8172 (2015).

[7] J. Yang, M. Guehr, T. Vecchione, M. S. Robinson, R. Li, N. Hartmann, X. Shen, R. Coffee, J. Corbett, A. Fry *et al.*, Diffractive imaging of a rotational wavepacket in nitrogen molecules with femtosecond megaelectronvolt electron pulses, Nat. Commun. **7**, 11232 (2016).

[8] J. Yang, M. Guehr, X. Shen, R. Li, T. Vecchione, R. N. Coffee, J. Corbett, A. Fry, N. Hartmann, C. Hast *et al.*, Diffractive Imaging of Coherent Nuclear Motion in Isolated Molecules, Phys. Rev. Lett. **117**, 153002 (2016).

[9] M. P. Minitti, J. M. Budarz, A. Kirrander, J. S. Robinson, D. Ratner, T. J. Lane, D. Zhu, J. M. Glownia, M. Kozina, H. T. Lemke *et al.*, Imaging Molecular Motion: Femtosecond X-Ray Scattering of an Electrocyclic Chemical Reaction, Phys. Rev. Lett. **114**, 255501 (2015).

[10] J. M. Glownia, A. Natan, J. P. Cryan, R. Hartsock, M. Kozina, M. P. Minitti, S. Nelson, J. Robinson, T. Sato, T. van Driel *et al.*, Self-Referenced Coherent Diffraction X-Ray Movie of Angstrom- and Femtosecond-Scale Atomic Motion, Phys. Rev. Lett. **117**, 153003 (2016).

[11] M. Meckel, D. Comtois, D. Zeidler, A. Staudte, D. Pavičić, H. C. Bandulet, H. Pépin, J. C. Kieffer, R. Dörner, D. M. Villeneuve, and P. B. Corkum, Laser-induced electron tunneling and diffraction, Science **320**, 1478 (2008).

[12] C. I. Blaga, J. Xu, A. D. DiChiara, E. Sistrunk, K. Zhang, P. Agostini, T. A. Miller, L. F. DiMauro, and C. D. Lin, Imaging ultrafast molecular dynamics with laser-induced electron diffraction, Nature (London) **483**, 194 (2012).

[13] M. G. Pullen, B. Wolter, A.-T. Le, M. Baudisch, M. Hemmer, A. Senftleben, C. D. Schröter, J. Ullrich, R. Moshammer, C. D. Lin, and J. Biegert, Imaging an aligned polyatomic molecule with laser-induced electron diffraction, Nat. Commun. **6**, 7262 (2015).

[14] J. Xu, C. I. Blaga, P. Agostini, and L. F. DiMauro, Time-resolved molecular imaging, J. Phys. B: At. Mol. Opt. Phys. **49**, 112001 (2016).

[15] R. Kanya, Y. Morimoto, and K. Yamanouchi, Observation of Laser-Assisted Electron-Atom Scattering in Femtosecond Intense Laser Fields, Phys. Rev. Lett. **105**, 123202 (2010).

[16] Y. Morimoto, R. Kanya, and K. Yamanouchi, Laser-assisted electron diffraction for femtosecond molecular imaging, J. Chem. Phys. **140**, 064201 (2014).

[17] N. M. Kroll and K. M. Watson, Charged-particle scattering in the presence of a strong electromagnetic wave, Phys. Rev. A **8**, 804 (1973).

[18] A. Weingartshofer and C. Jung, in *Multiphoton Ionization of Atoms*, edited by S. L. Chin and P. Lambropoulos (Academic, New York, 1984), Chap. 7, p. 155.

[19] N. J. Mason, Laser-assisted electron-atom collisions, Rep. Prog. Phys. **56**, 1275 (1993).

[20] A. Čerkić and D. B. Milošević, Few-cycle laser-pulse-assisted electron-atom potential scattering. Phys. Rev. A **87**, 033417 (2013).

[21] *International Table for X-Ray Crystallography*, edited by J. A. Ibers and W. C. Hamilton (The Kynoch Press, Birmingham, 1974), Vol. IV.

[22] R. Kanya, Y. Morimoto, and K. Yamanouchi, Apparatus for laser-assisted electron scattering in femtosecond intense laser fields. Rev. Sci. Instrum. **82**, 123105 (2011).

[23] Y. Morimoto, R. Kanya, and K. Yamanouchi, Light-Dressing Effect in Laser-Assisted Elastic Electron Scattering by Xe, Phys. Rev. Lett. **115**, 123201 (2015).

[24] L. S. Bartell and K. Kuchitsu, Significance of bond lengths determined by electron diffraction, J. Phys. Soc. Japan **17**, Suppl. B-II, 20 (1962).

[25] K. Yamanouchi, *Quantum Mechanics of Molecular Structures* (Springer-Verlag, Heidelberg, 2012).

[26] H. Hirori, A. Doi, F. Blanchard, and K. Tanaka, Single-cycle terahertz pulses with amplitudes exceeding 1 MV/cm generated by optical rectification in LiNbO$_3$, Appl. Phys. Lett. **98**, 091106 (2011).

[27] J. Hebling, G. Almási, I. Z. Kozma, and J. Kuhl, Velocity matching by pulse front tilting for large-area THz-pulse generation, Opt. Express **10**, 1161 (2002).

[28] P. R. Smith, D. H. Auston, and M. C. Nuss, Subpicosecond photoconducting dipole antennas, IEEE J. Quantum Electron. **24**, 255 (1988).

[29] D. H. Auston and M. C. Nuss, Electrooptic generation and detection of femtosecond electrical transients, IEEE J. Quantum Electron. **24**, 184 (1988).

[30] B. A. deHarak, L. Ladino, K. B. MacAdam, and N. L. S. Martin, High-energy electron-helium scattering in a Nd:YAG laser field, Phys. Rev. A **83**, 022706 (2011).

[31] B. A. deHarak, B. Nosarzewski, M. Siavashpouri, and N. L. S. Martin, Electron-helium scattering in a 1.17 eV laser field: The effect of polarization direction, Phys. Rev. A **90**, 032709 (2014).

[32] N. L. S. Martin and B. A. deHarak, Test of target independence for free-free scattering in a Nd:YAG laser field, Phys. Rev. A **93**, 013403 (2016).

[33] B. A. deHarak, B. N. Kim, C. M. Weaver, N. L. S. Martin, M. Siavashpouri, and B. Nosarzewski, Effects of polarization direction on laser-assisted free–free scattering, Plasma Sources Sci. Technol. **25**, 035021 (2016).

[34] J. Itatani, F. Quéré, G. L. Yudin, M. Yu. Ivanov, F. Krausz, and P. B. Corkum, Attosecond Streak Camera, Phys. Rev. Lett. **88**, 173903 (2002).

[35] M. Kitzler, N. Milosevic, A. Scrinzi, F. Krausz, and T. Brabec, Quantum Theory of Attosecond XUV Pulse Measurement by Laser Dressed Photoionization, Phys. Rev. Lett. **88**, 173904 (2002).